Space Weather

RESEARCH ARTICLE
10.1029/2020SW002685

Modeling of Planetary Wave Influences on the Pre-reversal Enhancement of the Equatorial F Region Vertical Plasma Drift

Y. Yamazaki[1] and C. Diéval[1]

[1]Department of Geophysics, Deutsche GeoForschungsZentrum, Potsdam, Germany

Key Points:

- Quiet-time day-to-day and longitudinal variability of the pre-reversal enhancement (PRE) in the equatorial vertical plasma drift is examined
- Planetary-wave influences on PRE are evaluated for the first time using global simulations
- Quasi-6-day wave can lead to ~6-day oscillations in the PRE intensity with zonal wavenumber 1.

Correspondence to:
Y. Yamazaki,
yamazaki@gfz-potsdam.de

Citation:
Yamazaki, Y., & Diéval, C. (2021). Modeling of planetary wave influences on the pre-reversal enhancement of the equatorial F region vertical plasma drift. *Space Weather*, *19*, e2020SW002685. https://doi.org/10.1029/2020SW002685

Received 19 NOV 2020
Accepted 30 JAN 2021

Abstract Temporal and longitudinal variations of the pre-reversal enhancement (PRE) in the equatorial F region vertical plasma drift are examined based on idealized simulations by the thermosphere-ionosphere-electrodynamics general circulation model performed under geomagnetically quiet ($Kp = 1$) and high solar-flux ($F_{10.7} = 200$) conditions. The model takes into account forcing by large-scale waves from the middle and lower atmosphere, which leads to day-to-day variations of PRE. Simulations are performed under different wave forcing in order to separate contributions of various types of waves. It is shown that the simulated day-to-day variability of the PRE intensity is predominantly due to forcing by waves with periods less than 2 days, that is, tides and their modulation. Planetary-wave forcing (periods of 2–20 days) makes contributions to periodic oscillations in the PRE intensity. Especially, the westward-propagating quasi-6-day wave (Q6DW) with zonal wavenumber 1 is found to be an important source of ~6-day oscillations of PRE. Not only the Q6DW from below but also the Q6DW generated within the thermosphere, as well as the secondary waves due to the nonlinear interaction between the Q6DW and migrating tides, is at play. The zonal wavenumber 1 nature of the ~6-day oscillations could contribute to longitudinal differences in the appearance of equatorial spread F and plasma bubbles, which are strongly controlled by PRE.

1. Introduction

The $\mathbf{E} \times \mathbf{B}$ drift dominates the plasma motion across magnetic field lines in the F region ionosphere. In the equatorial region, the quiet-time dynamo electric field is usually eastward during the day and westward during the night (e.g., A. D. Richmond, 1995), and thus the F-region vertical plasma drift is upward during the day and downward during the night (e.g., Fejer et al., 2008a; Scherliess & Fejer, 1999). Around the sunset time, the upward drift velocity (V_Z) often shows a rapid increase before the reversal to downward flow (Woodman, 1970). This phenomenon is known as the "pre-reversal enhancement (PRE)" in the equatorial vertical plasma drift. PRE is frequently observed during solar maximum while it is small or absent during solar minimum (e.g., Fejer et al., 1991; Madhav Haridas et al., 2015; Stoneback et al., 2011). The strong upward drift due to PRE has been identified as a determining factor for the appearance of the equatorial spread F (Fejer et al., 1999; Hysell & Burcham, 2002) and equatorial plasma bubbles (Huang & Hairston, 2015; Kil et al., 2009; Stolle et al., 2008), which can cause radio wave scintillations and hence are major space weather concerns.

The production mechanism of PRE has been explained in terms of the F-region dynamo and its electrodynamic coupling to the E region (e.g., Eccles, 1998; Farley et al., 1986; Heelis et al., 1974; Rishbeth, 1971). Eccles et al. (2015), reviewing various contributing mechanisms, concluded that PRE is primarily due to the curl-free nature of the electric field. Below is a brief summary of the curl-free mechanism. The polarization electric field due to the F-region dynamo can be approximated in the following formula (e.g., Heelis, 2004):

$$\mathbf{E} = -\frac{\Sigma_P^F}{\Sigma_P^E + \Sigma_P^F}\mathbf{U}_F \times \mathbf{B}, \tag{1}$$

where $\mathbf{E}$ is the electric field, $\mathbf{U}_F$ is the F-region wind velocity, $\mathbf{B}$ is the Earth's main magnetic field, and Σ_P^F and Σ_P^E are field-line-integrated F- and E-region Pedersen conductivities, respectively. During the daytime, the E-region conductivity is much larger than the F-region conductivity, and thus the polarization electric

field due to the F-region dynamo can be ignored. During sunset hours, the E-region conductivity decays rapidly, and the F-region dynamo becomes proportionally more important. The F-region wind is eastward around the sunset time, thus the associated electric field is downward in the equatorial region. The strength of the downward electric field is not uniform in the zonal direction but has a strong eastward gradient (i.e., it increases toward the night side) because of the rapid decay of the E-region conductivity and the eastward acceleration of the F-region wind around the sunset time. However, the curl of the electric field must be zero. This requirement leads to an eastward electric field, and it is this eastward electric field that corresponds to the large upward vertical drift of PRE.

The maximum V_Z of PRE (hereafter PRE intensity) varies with season, and the seasonal pattern is different at different longitudes (Abdu et al., 1981; Batista et al., 1986; Fejer et al., 2008a). The seasonal and longitudinal dependence of PRE arises from the longitudinal variation of the magnetic declination and the seasonal variation in the angle (denoted here as α) between the sunset terminator and magnetic field (e.g., Eccles et al., 2015). As can be understood from the production mechanism of PRE described above, the PRE intensity depends on the zonal gradient of the field-line-integrated E-region conductivity across the sunset terminator, in other words the duration of the combined E-region sunsets. At longitudes where the sunset terminator is in alignment with the magnetic meridian (i.e., $\alpha = 0°$), the E-region sunset takes place simultaneously in the northern and southern hemispheres, thus the decay of the field-line-integrated E-region conductivity is relatively fast. At longitudes where α is nonzero, the decay of the field-line-integrated E-region conductivity is slower because of the time lag in the E-region sunsets between the two hemispheres. Since the α angle changes with season and longitude, the PRE intensity is seasonally and longitudinally dependent. The α-angle control of the evening ionosphere was first proposed by Tsunoda (1985) to explain the climatology of spread F.

The PRE intensity also changes from day-to-day. The day-to-day variability is partly due to changes in geomagnetic activity (Fejer et al., 2008b; Fejer & Scherliess, 1997). The disturbance dynamo electric field (Blanc & Richmond, 1980) and the prompt penetration electric field from the polar region (Kelley et al., 1979; Nishida, 1968) are responsible for geomagnetic activity effects on PRE. The day-to-day variability is also present in PRE during geomagnetically quiet periods (Fejer & Scherliess, 2001). The quiet-time day-to-day variability of PRE is generally attributed to atmospheric forcing from below. The neutral atmosphere at altitudes of the E- and F-region ionosphere, say 90–600 km, is highly variable due to forcing by various types of waves that propagate from the middle and lower atmosphere (e.g., Liu, 2016). Recently, Liu (2020) presented simulation results based on the whole atmosphere model, WACCM-X 2.0 (Liu et al., 2018), which takes into account forcing by large-scale waves such as tides and planetary waves. They were able to reproduce the day-to-day variability of PRE V_Z with realistic amplitude (3–6 m/s in standard deviation) under geomagnetically quiet ($Kp = 0.33$) and high solar-flux ($F_{10.7} = 200$) conditions, thus establishing the role of large-scale waves for the day-to-day variability of PRE. Ghosh et al. (2020) also reported day-to-day variations of PRE reproduced by another whole atmosphere model, GAIA (Jin et al., 2011).

The present study also uses a numerical model, namely, the thermosphere-ionosphere-electrodynamics general circulation model (TIE-GCM) (Qian et al., 2014; Richmond et al., 1992). The primary objective is to evaluate the role of planetary waves with periods of 2–20 days (Forbes, 1995; Salby, 1984) in producing the day-to-day variability of PRE. This is motivated by studies based on radar observations that have frequently detected periodic oscillations in PRE V_Z within this period range (e.g., Abdu et al., 2006a; Abdu, Ramkumar, 2006b; Bertoni et al., 2011; de Abreu et al., 2014; Manju & Aswathy, 2020; Zhu et al., 2017). For example, Abdu et al. (2006a) observed oscillations with periods of 2–7 days simultaneously in PRE and mesospheric winds. In studies by ground-based observations, however, it is difficult to determine the global nature of PRE oscillations (e.g., zonal wavenumber) due to limited longitudinal coverage. We will overcome this issue using model outputs from all longitudes, and present, for the first time, spectra of PRE oscillations for different zonal wavenumbers. Also, in observational studies, it is difficult to separate contributions of planetary waves and tides in daily values of PRE. We will address the relative importance of planetary waves and tides in periodic oscillations of PRE by comparing simulations performed under different wave forcing. Moreover, multi-day oscillations of PRE in observational data can result not only from atmospheric waves but also from oscillations in solar and geomagnetic activity. This ambiguity will be avoided in our idealized simulations that assume constant solar and geomagnetic activity.

This study is also motivated by renewed interest in planetary-wave influences on the ionosphere in general owing to recent progress in the subject based on global satellite observations (e.g., Gan et al., 2020; Gu et al., 2018; Yamazaki et al., 2018) as well as advances in the understanding of the underlying processes by dedicated modeling work (e.g., Forbes et al., 2018b; Forbes et al., 2018a; Gan et al., 2017; Miyoshi & Yamazaki, 2020). Most modeling studies on the planetary-wave effects on the ionosphere have been conducted under solar minimum conditions, for which PRE is negligibly small. The present study is unique in examining the ionospheric response to planetary waves for high solar-flux conditions with a special focus on PRE.

2. Model and Numerical Experiments

The TIE-GCM is a physics-based global three-dimensional model of the coupled ionosphere-thermosphere system (Qian et al., 2014; Richmond et al., 1992). For the present study, we use version 2.0 of the TIE-GCM with horizontal resolution of 2.5 × 2.5° in geographic longitude and latitude. The vertical coordinate of the TIE-GCM is defined as $Z = \ln(p_0/p)$, where p is the pressure and p_0 ($=5 \times 10^{-7}$ hPa) is the reference pressure. The model extends from $Z = -7$ (~97 km altitude) to $Z = 7$ (~700 km for solar maximum conditions) with vertical resolution of $\Delta Z = 0.25$. The electrodynamics is calculated in the Magnetic Apex coordinate system (A. Richmond, 1995) with a realistic geomagnetic field configuration specified by the International Geomagnetic Reference Field (IGRF-12) (Thébault et al., 2015). Geomagnetic activity and solar activity can be specified using the Kp and $F_{10.7}$ indices, respectively. All simulations presented in this study were performed under geomagnetically quiet ($Kp = 1$) and high solar-flux ($F_{10.7} = 200$) conditions.

Effects of upward propagating waves from the middle and lower atmosphere can be introduced by specifying the lower boundary. For this study, the lower boundary of the TIE-GCM was constrained using horizontal winds, geopotential height, and temperature at 97 km from another model called the thermosphere ionosphere mesosphere electrodynamics general circulation model (TIME-GCM) (Roble & Ridley, 1994), which itself is constrained at 30 km with 3-hourly outputs from the Modern Era Retrospective-analysis for Research and Applications (MERRA) (Rienecker et al., 2011). The method of constraining the TIE-GCM lower boundary with TIME-GCM/MERRA data is described in detail by Maute (2017), and we used the same lower-boundary fields as Maute (2017), which are based on the MERRA data for the year 2009. The use of the MERRA data for the solar minimum year of 2009 in our TIE-GCM simulations for high solar-flux conditions is justified by the fact that planetary waves and tides observed in the middle atmosphere below 97 km show little dependence on solar activity (Oberheide et al., 2009; Yamazaki, 2018). Koval et al. (2018) numerically showed that solar activity can affect planetary waves with periods of 4–16 days only above 100 km.

The lower boundary fields given by the TIME-GCM/MERRA data are separated into two parts. One is the daily zonal mean and the other is perturbations from the daily zonal mean. The former contains zonally symmetric (S0) oscillations at planetary-wave periods (e.g., Pancheva et al., 2009; Forbes et al., 2018b) while the latter contains eastward- and westward-propagating planetary waves and tides. We ran three cases of simulations with slightly different lower-boundary conditions. The first case is referred to as "*reference*" and uses the original values of the zonal mean and perturbation fields. The model results presented in this paper are from the *reference* simulation unless otherwise noted. In the second case, which is referred to as "*no_PW*," planetary waves are excluded from the lower-boundary fields by applying a high-pass filter with a cut-off period of 2 days only to the perturbation fields. In this way, eastward- and westward-propagating waves with periods longer than 2 days are removed from the perturbation fields while multi-day oscillations in the zonal mean fields are retained. The third case, referred to as "*tides_only*," uses the same perturbation fields as the *no_PW* simulation but additionally, a low-pass filter is used to remove the S0 oscillations with periods less than 100 days. In this way, variations at planetary-wave periods are removed from both the daily zonal mean fields and perturbation fields while retaining seasonal variations, which are dominated by the annual (365 days) and semiannual (182.5 days) components. Waves with periods less than 2 days in the lower thermosphere can be largely attributed to tides and their modulation through the interaction with other large-scale waves (e.g., Nystrom et al., 2018). The lower boundary conditions for the three cases are summarized in Table 1.

Table 1
Simulated Cases and Differences

Case #	Case name	LB (zonal mean)	LB (perturbations)
(1)	*reference*	TIME-GCM/MERRA	TIME-GCM/MERRA
(2)	*no_PW*	TIME-GCM/MERRA	<2 days
(3)	*tides_only*	>100 days	<2 days
(1)−(2)	*PW_contribution*		
(2)−(3)	*S0_contribution*		

Abbreviation: LB, Lower Boundary

Differences in the results obtained from a selected pair of cases can highlight contributions of certain wave forcing mechanisms. For instance, the differences between the *reference* and *no_PW* simulations isolate the effect of planetary-wave forcing at 97 km, and hence are referred to as "*PW_contribution*." Similarly, the differences between the *no_PW* and *tides_only* simulations isolate the effect of S0 forcing at 97 km, and are referred to as "*S0_contribution*." Detailed discussion will be presented later regarding what waves are included in each case listed in Table 1 and how they could contribute to planetary-wave oscillations in PRE.

The three cases of simulations were run for the entire year from January 1 to December 31. The simulation time step was set to 15 s, and the vertical plasma drift velocity V_Z was output every 5 min in model time, along with other diagnostic fields. The high sampling rate of the vertical plasma drift velocity helps to accurately determine the time and intensity of PRE. Our PRE detecting routine involves three steps. First, the V_Z data at the magnetic equator at an altitude of 346.5 km were plotted as a function of local time for each day. Second, local maxima were searched in V_Z between 1 h before and after the time of the E-region sunset at 110 km over the magnetic equator. Finally, the local maximum with the largest V_Z was selected as PRE. PRE was sometimes detected after the vertical drift turns downward in the afternoon. Although, strictly speaking, these cases are not "pre-reversal" enhancement, they are kept in our PRE data. Accordingly, the PRE intensity can be a negative value, although such cases are not common. Also sometimes, no local maximum was detected within the said local-time range. In this case, no values were assigned to the intensity and local time of PRE. The PRE data from the *reference*, *no_PW* and *tides_only* simulations are archived at GFZ Data Services (Yamazaki & Dieval, 2021).

Figure 1 presents two examples of V_Z data plotted as a function of local time. In Figure 1a, a local maximum is found around the time of the E-region sunset. The purple vertical lines indicate ±1 h from the E-region sunset time at the magnetic equator. The intensity and local time of PRE are 18.7 m/s and 19.08 h, respectively. The pattern of the daily variation of V_Z is in good agreement with those typically observed during solar maximum (e.g., Fejer et al., 1991; Scherliess & Fejer, 1999). Previous studies also found that the TIE-GCM is capable of reproducing observed features of the daily variation in V_Z including PRE (e.g., Fesen et al., 2000; Heelis et al., 2012; Vichare & Richmond, 2005). Figure 1b shows a case where no PRE was detected.

3. Results

3.1. Seasonal and Longitudinal Dependence

Daily values of the PRE intensity are plotted in Figure 2a as a function of longitude and day of year (DoY). The PRE intensity exhibits both day-to-day and seasonal variations at a given longitude. At a fixed DoY, the PRE intensity is longitudinally dependent. The seasonal and longitudinal dependence is more clearly visible in Figure 2b where temporal and spatial averaging is applied to the PRE intensity with a 30-day time and 15° longitude window. The obtained seasonal and longitudinal pattern resembles those derived from satellite measurements (e.g., Huang & Hairston, 2015; Kil et al., 2009). As mentioned earlier, the seasonal and longitudinal dependence of the PRE intensity is generally attributed to changes in the α angle between the sunset terminator and horizontal magnetic field. Figure 2c depicts the seasonal and longitudinal dependence of the α angle. A comparison between Figures 2b and 2c shows the expected anti-correlation between

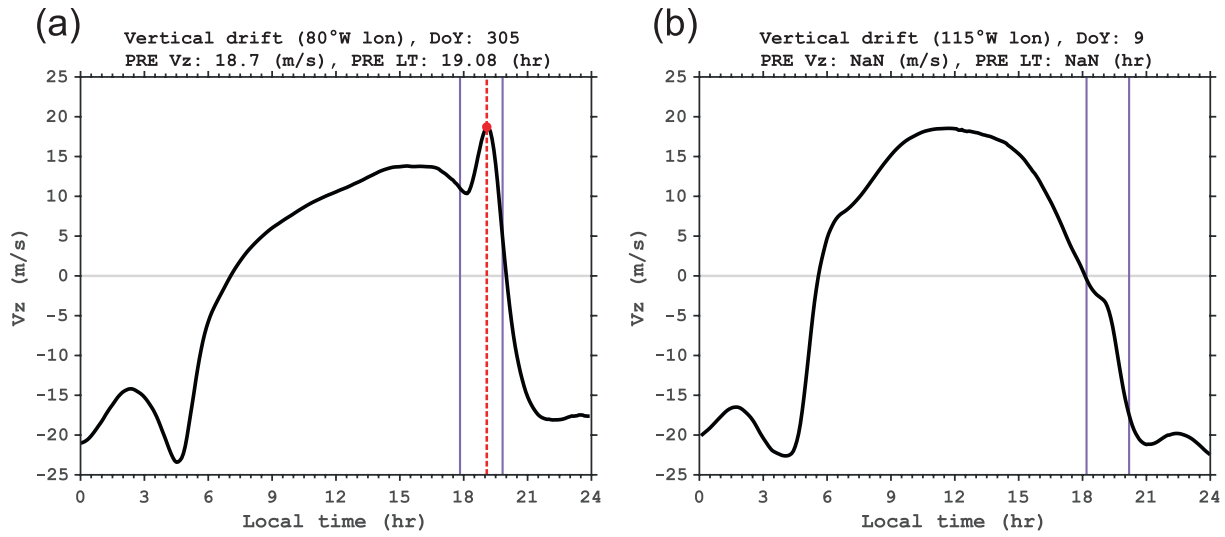

Figure 1. Daily variations of the equatorial vertical plasma drift V_Z at an altitude of 346.5 km at (a) 80°W longitude on DoY = 305 and (b) 115°W longitude on DoY = 9. The purple vertical lines indicate ±1 h from the sunset time at 110 km. In the left panel, the vertical red dashed line indicates the time for the maximum PRE in V_Z.

the PRE intensity and α angle. It is noted that the PRE intensity at a fixed DoY often shows a longitudinal variation with 4–8 peaks. Such variations are not necessarily associated with the α angle, which shows smoother longitudinal variations. Atmospheric waves with different zonal wavenumbers can contribute to longitudinal variations in ionospheric parameters. For example, the eastward-propagating diurnal tide with zonal wavenumber 3 is known to be a source of the four-peak longitudinal structure of the low-latitude ionosphere (e.g., Lühr & Manoj, 2013; Pancheva & Mukhtarov, 2010). Figure 2d displays the standard deviation of the PRE intensity computed within the 30-day time and 15° longitude window after the removal of the smoothed seasonal and longitudinal variations shown in Figure 2b. The value of the standard deviation is 5.6 (±1.0) m/s on average, while it can be as large as 9 m/s at certain times and longitudes.

Figure 2e is the same as Figure 2a except for the local time of PRE. It is seen that the local time of PRE also varies with DoY and longitude. It exhibits both day-to-day and seasonal variations at a given longitude. To our knowledge, this is the first time that day-to-day variations of the PRE local time due to atmospheric forcing are reproduced by a global model. At a fixed DoY, the PRE local time is longitudinally dependent. The pattern of the seasonal and longitudinal variations shown in Figure 2f, obtained by temporal and spatial averaging as in Figure 2b is different from that of the PRE intensity (Figure 2b). The mean value of the PRE local time is 18.8 h. Figure 2g shows the seasonal and longitudinal dependence of the sunset time at 110 km at the magnetic equator. The PRE local time is seen to follow the seasonal and longitudinal variations of the E-region sunset time. Earlier, Kil and Oh (2011), using satellite observations, reported that the longitudinal variation of the PRE local time depends on the longitudinal variation of the E-region sunset time. Our simulation results confirm their finding. Figure 2h shows the standard deviation of the PRE local time calculated in the same way as the standard deviation of the PRE intensity in Figure 2d. The mean value of the standard deviation is 7.9 (±3.6) min, which is rather small given that the time resolution of our simulation output is 5 min. Thus, for the remainder of the paper, we focus on the behavior of the PRE intensity.

3.2. Planetary-Wave Influences: Ground Observer Perspective

We now examine the day-to-day variability of the PRE intensity from the perspective of ground observers. Figures 3a and 3d present time series of PRE intensity at selected longitudes (60°E and 180°E). In both figures, the green line shows daily values from the *reference* simulation and the black line is from the *tides_only* simulation, where the lower boundary fields exclude long-period (>2 days) oscillations except the seasonal variation of the zonal mean (see Table 1). The *tides_only* results represent the contributions of tides (24, 12, 8 h, ...) and their modulation through the interaction with other waves. The good agreement between the

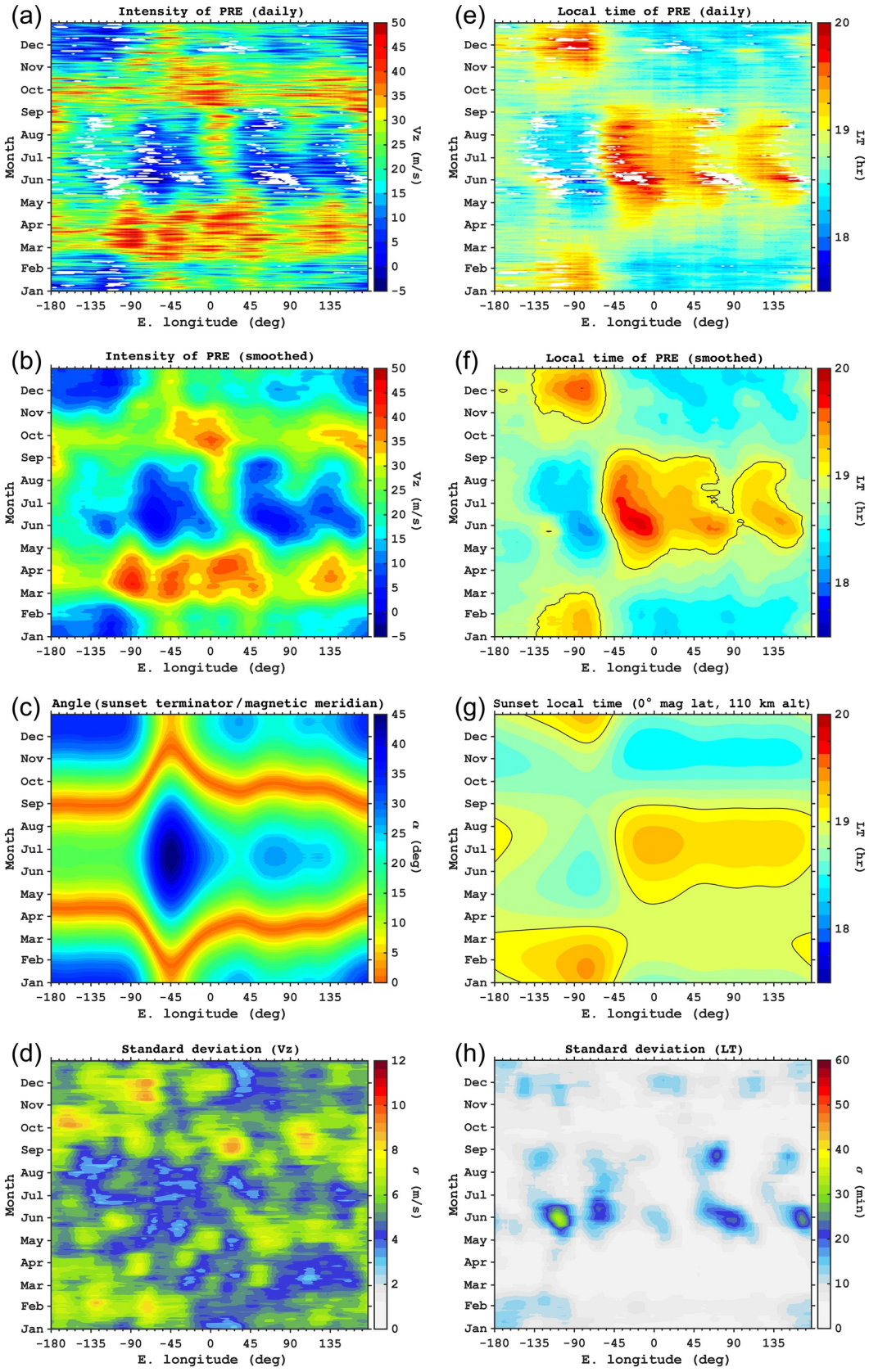
(a)
Intensity of PRE (daily)
(b)
Intensity of PRE (smoothed)
(c)
Angle (sunset terminator / magnetic meridian)
(d)
Standard deviation (Vz)
(e)
Local time of PRE (daily)
(f)
Local time of PRE (smoothed)
(g)
Sunset local time (0° mag lat, 110 km alt)
(h)
Standard deviation (LT)
Month
Dec
Nov
Oct
Sep
Aug
Jul
Jun
May
Apr
Mar
Feb
Jan
-180 -135 -90 -45 0 45 90 135
E. longitude (deg)
Vz (m/s)
α (deg)
LT (hr)
σ (m/s)
σ (min)

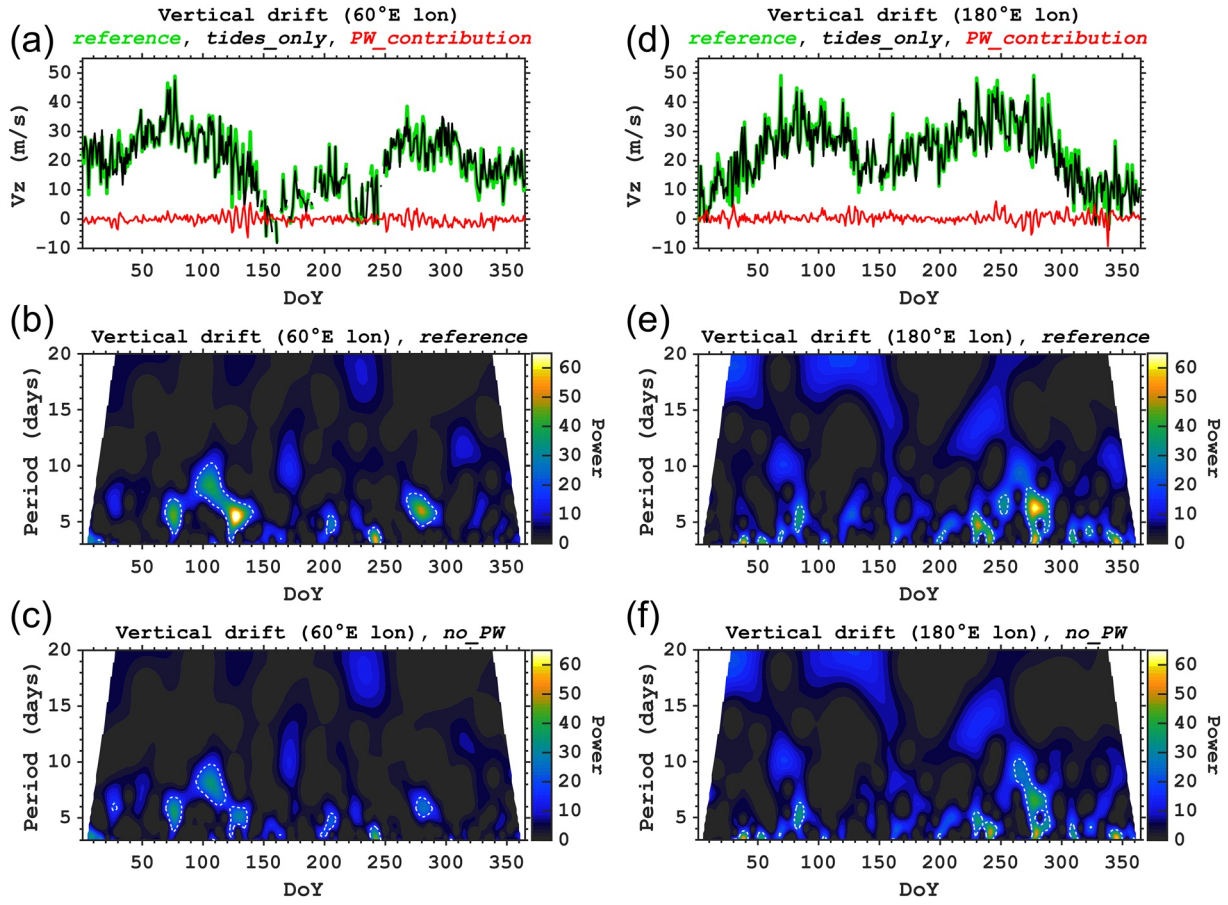

Figure 3. Intensity of the pre-reversal enhancement (PRE) in the equatorial F-region vertical plasma drift at (a–c) 60°E longitude and (d–f) 180°E longitude. Panels (a and d) show time series of the PRE intensity for the *reference* simulation (green lines), *tides_only* simulation (black lines), and *PW_contribution* case (red lines). Panels (b and e) show the wavelet spectrum of the PRE intensity for the *reference* simulation. Panels (c and f) show the wavelet spectrum of the PRE intensity for the *no_PW* simulation. See Table 1 for the description of different simulation cases. In panels (b, c, e, and f), the 95% confidence level is indicated by the white dashed line.

reference and *tides_only* results indicate that the variability of PRE V_Z is primarily due to tidal-wave forcing. The day-to-day variability associated with planetary-wave forcing is isolated in the *PW_contribution* results, which are indicated by the red lines in Figures 3a and 3d. The changes in the PRE intensity due to planetary waves are generally smaller than those associated with tidal waves, but occasionally, they become comparable when the planetary-wave contribution is enhanced (e.g., DoY from 120 to 140 in Figure 3a).

Figures 3b and 3e show Morlet wavelet power spectra of the PRE intensity at the two locations as derived from the *reference* simulation. In previous observational studies, wavelet spectra have frequently been used to detect planetary-wave signatures in PRE (e.g., Abdu, Batista, et al., 2006). At 60°E longitude (Figure 3b), the strongest wave signal is seen at a period of 5–6 days around DoY = 120–130. At 180°E longitude (Figure 3e), the 5–6-day oscillation around DoY = 120–130 is not as prominent but a strong wave signal is seen at ~6 day around DoY = 270–280. Figures 3c and 3f show similar results but for the *no_PW* simulation, which excludes traveling planetary waves with periods longer than 2 days at the lower boundary of the model (97 km). In this case, ~6-day signatures around DoY = 120–130 and DoY = 270–280 are weakened but remain significant. The results suggest that planetary-wave forcing makes an important contribution

Figure 2. Longitude and seasonal dependence of the pre-reversal enhancement (PRE) in the equatorial vertical plasma drift: (a) daily values of the PRE intensity, (b) temporally and spatially smoothed PRE intensity with a 30-days time and 15° longitude window, (c) angle α between the sunset terminator and magnetic meridian at an altitude of 110 km, (d) standard deviation of daily PRE intensities obtained with the 30-day time and 15° longitude window, (e) daily values of the PRE local time, (f) temporally and spatially smoothed PRE local time, (g) sunset time at 110 km over the magnetic equator, and (h) standard deviation of daily PRE local times. The black contour lines in (f and g) correspond to 19.0 h local time.

to periodic oscillations (in particular those with periods of ~6 days) in PRE V_Z observed from the ground. The results also suggest that ~6-day oscillations result not only from planetary waves but also from other processes such as tidal modulation by planetary waves. Considering all longitudes, the amplitudes of ~6-day oscillations in PRE intensity are 5.2 ± 1.8 m/s around DoY = 120–130 and 6.0 ± 2.4 m/s around DoY = 270–280 from the ground-observer perspective.

3.3. Planetary-Wave Influences: Global Perspective

The zonal structure of planetary-wave oscillations in the PRE intensity is examined using simulation results, which cover all longitudes. Fourier spectra (e.g., Wu et al., 1993) of the PRE intensity are presented in Figures 4a–4e for W2, W1, S0, E1, and E2, where "W" and "E" represent westward- and eastward-propagating components, respectively, and the number following W or E indicates the zonal wavenumber. As mentioned earlier, S0 signifies the zonal-mean oscillation. The rich spectra of W2, W1, and E1 contribute to the complex day-to-day variability of the PRE intensity. The largest contribution to the PRE intensity oscillations at periods of 2–20 days comes from the W1 component (i.e., westward-propagating oscillations with zonal wavenumber 1). Especially, ~6-day oscillations are prominent around DoY = 120–140 and DoY = 270–290, during which wavelet spectra at fixed longitudes show ~6-day peaks (Figures 3b and 3e). The maximum amplitude of the ~6-day oscillation in the W1 component exceeds 4 m/s.

Fourier spectra of the zonal wind over the equator at the TIE-GCM lower boundary (97 km) are presented in Figures 4f–4j for W2, W1, S0, E1, and E2. Enhanced W1 activity at periods of ~6 days is seen around DoY = 120–140 and DoY = 270–290, which is likely associated with the so-called quasi-6-day wave (Q6DW) (e.g., Gan et al., 2018; Liu et al., 2004). Gu et al. (2018) reported the Q6DW with the zonal wind amplitude of up to ~25 m/s over the equator based on satellite data at altitudes of 90–100 km for the year 2009. Our TIE-GCM results, which are constrained with the TIME-GCM/MERRA output for the same year, are in agreement with the observations of Gu et al. (2018). Q6DW signatures are also found at other latitudes but with smaller amplitudes (not shown here). The meridional structure of the Q6DW is known to be similar to that of the (1,1) Rossby normal mode, which has the maximum zonal wind perturbation over the equator (e.g., Gu et al., 2018; Wu et al., 1994). It is noted that the Q6DW in 2009 is not particularly strong, and a similar level of Q6DW activity has been observed in the mesosphere and lower thermosphere (MLT) region in other years including both solar minimum and solar maximum (e.g., Qin et al., 2019; Yamazaki, 2018).

A comparison of Figure 4g with Figure 4b suggests a link between the Q6DW and ~6-day oscillations in the W1 component of the PRE intensity. Apart from the Q6DW, there is some S0 activity in the equatorial zonal wind at periods of 8–9 days around DoY = 260–270 and 14–15 days around DoY = 340–350 (Figure 4h), but no similar S0 oscillations are seen in the PRE intensity (Figure 4c). W2 and E1 wave activities are relatively weak for the equatorial zonal wind (Figures 4f and 4i), unlike those of the PRE intensity, for which the amplitude frequently exceeds 2 m/s (Figures 4a and 4d).

Figure 5 shows W1 spectra of the PRE intensity similar to Figure 4b but for different simulation cases (see Table 1). The *tides_only* simulation (Figure 5a) reproduces most W1 activities in the *reference* simulation (Figure 4b), except for ~6-day oscillations around DoY = 120–140 and DoY = 270–290, which are stronger in the *PW_contribution* case (Figure 5b). The W1 amplitude is small (<1 m/s) in the *S0_contribution* case.

4. Discussion

Our simulation results reveal westward-propagating ~6-day oscillations with zonal wavenumber 1 (hereafter referred to as " ~6-day oscillations" for brevity) in the PRE intensity during times of enhanced Q6DW activity. The Q6DW is one of the planetary waves that are commonly observed in the MLT region around equinoctial months (e.g., Forbes & Zhang, 2017; Talaat et al., 2001; Wu et al., 1994). The wave is often regarded as the manifestation of the (1,1) Rossby normal mode of classical wave theory. It is known that the Q6DW can lead to ~6-day oscillations in the equatorial electrojet (Yamazaki et al., 2018, 2020) and low-latitude F-region plasma density (Gu et al., 2018; Lin et al., 2020) by modulating the daytime dynamo electric field (Gan et al., 2016). The present study provides evidence that the Q6DW is also important for the evening ionospheric electrodynamics. Below we discuss the connection between Q6DW activity in the MLT region and ~6-day oscillations in PRE.

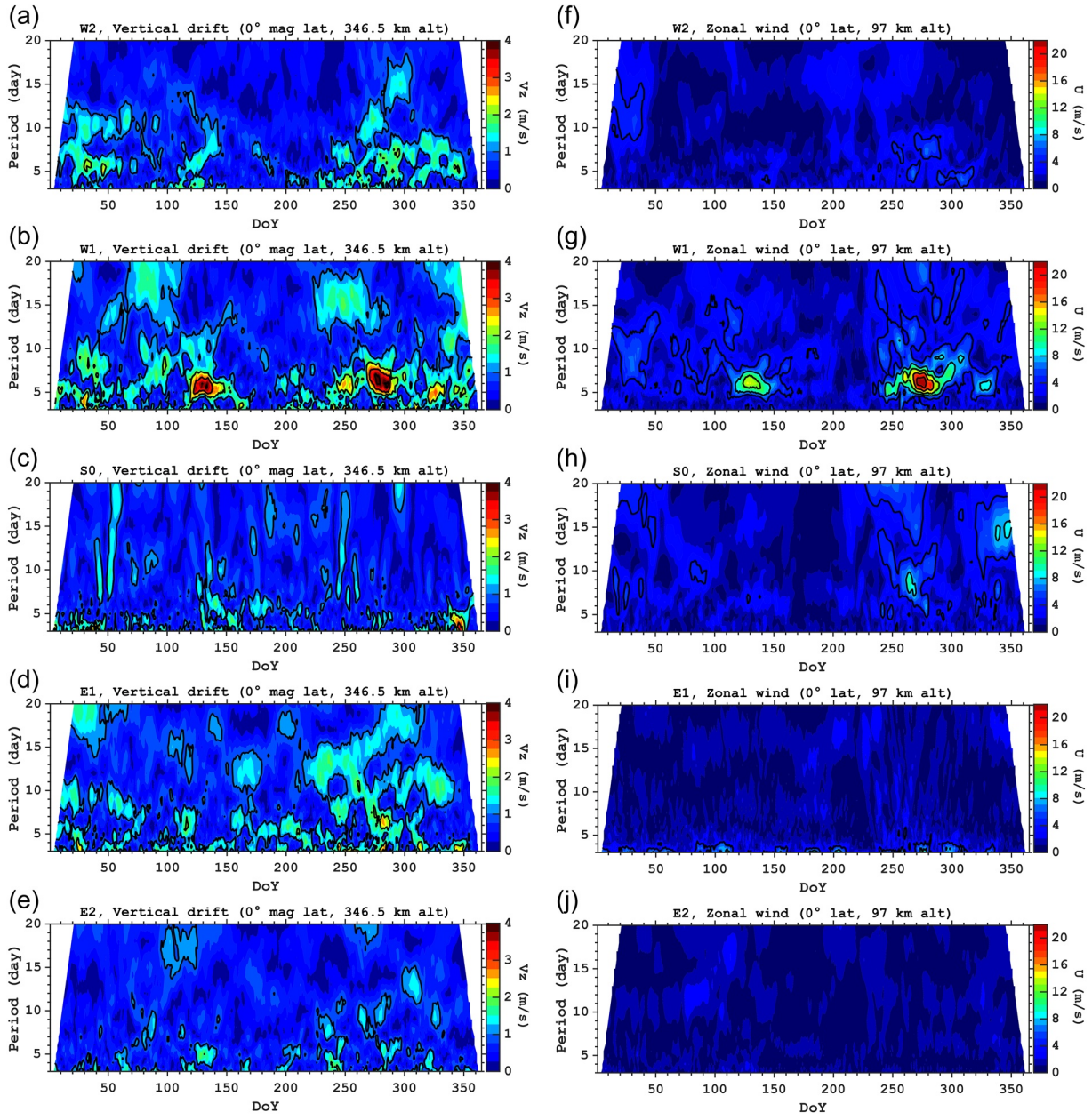

Figure 4. Day of year versus period spectra for (a–e) the intensity of the pre-reversal enhancement (PRE) in the equatorial F-region vertical plasma drift and (f–j) the zonal wind over the equator at the lower boundary of the model (97 km). Panels (a and f) are for the westward-propagating component with zonal wavenumber 2; (b and g) are for the westward-propagating component with zonal wavenumber 1; (c and h) are for the zonally symmetric oscillations; (d and i) are for the eastward-propagating component with zonal wavenumber 1; and (e and j) are for the eastward-propagating component with zonal wavenumber 2.

We address the issue of possible aliasing into planetary-wave spectra of PRE V_Z (Figures 4a–4e). Given the small range of local time within which PRE occurs (Figure 2e), it can be safely assumed that the local time of PRE (t_{LT} in units of days) is a fixed value and does not vary with DoY or longitude. The local time can be expressed using the universal time (t_{UT} in days) and longitude (λ in radians). That is,

$$t_{LT} = t_{UT} + \frac{\lambda}{\Omega}, \tag{2}$$

where Ω is the rotation rate of the Earth ($=2\pi$ per day). A planetary wave with zonal wavenumber s and frequency ω (cycles per day) can be expressed as

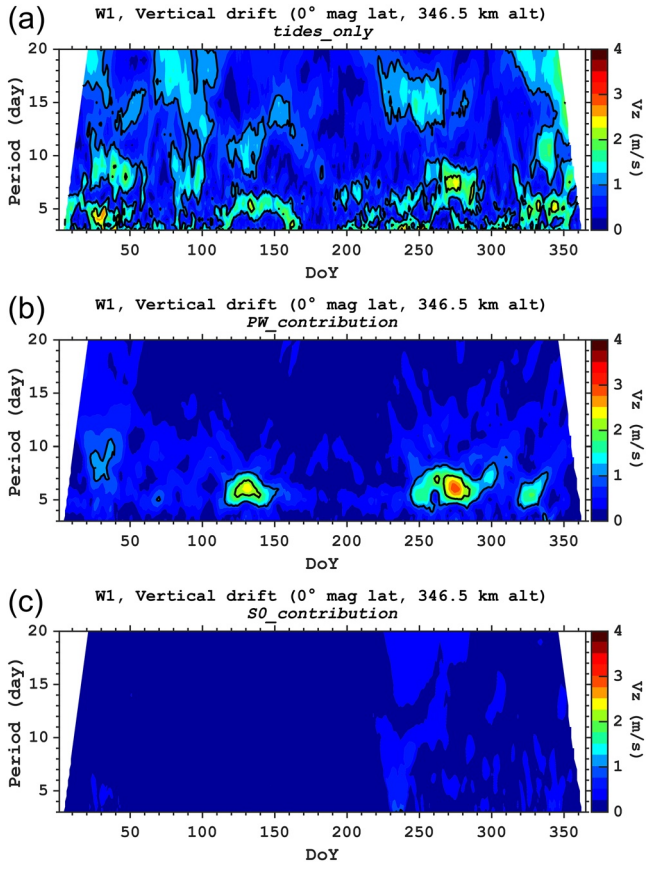

Figure 5. Same as Figure 4b except for (a) the *tides_only*, (b) *PW_contribution*, and (c) *S0_contribution* cases. See Table 1 for the description of different simulation cases.

Table 2
Waves That Can Alias Into ~6-Day Oscillations in the Fixed Local Time Frame

Zonal wavenumber s	Frequency (ω/days)	Period τ (days)	Possible source
0	0.83	1.2	Q6DW ×DW1$_{(-)}$
+1	1.83	0.55	Q6DW ×SW2$_{(-)}$
+2	1.17	0.86	Q6DW ×DW1$_{(+)}$
+2	2.83	0.35	Q6DW ×TW3$_{(-)}$
+3	2.17	0.46	Q6DW ×SW2$_{(+)}$
+3	3.83	0.26	Q6DW ×QW4$_{(-)}$

Note. They can be secondary waves resulting from the interaction of the Q6DW and a migrating tide, which are listed as "possible source" (fourth Column). The " + " ("−") sign in the fourth column indicates that the wavenumber and frequency of the secondary wave is the sum (difference) of the wavenumbers and frequencies of the interacting waves. Only the waves with $|s| < 4$ are Listed here. Q6DW = quasi-6-day wave. DW1 = Migrating diurnal tide. SW2 = Migrating semidiurnal tide. TW3 = Migrating terdiurnal tide. QW4 = Migrating quatradiurnal tide.

$$A\cos\left(\omega\Omega t_{UT} + s\lambda - \phi\right), \tag{3}$$

where A and ϕ are the amplitude and phase of the wave, respectively. The wave propagates westward if $s > 0$ and eastward if $s < 0$. For the Q6DW, $s = s_6$ (= + 1) and $\omega = \omega_6$ (= ~1/6). Thus, eliminating λ in (3) with Equation (2), the Q6DW is

$$A\cos\left[\left(s_6 - \omega_6\right)\Omega t_{UT} - \phi'\right], \tag{4}$$

where

$$\phi' = s_6 t_{LT}\Omega - \phi. \tag{5}$$

Since t_{LT} is a fixed value, (4) is a function of t_{UT} only and is a simple cosine wave with the frequency of $s_6 - \omega_6$ cycles per day. Therefore, in the fixed local time frame, any wave with the zonal wavenumber s and frequency ω that satisfies the following relationship is a potential source of aliasing into ~6-day oscillations of PRE:

$$\left|s - \omega\right| = s_6 - \omega_6. \tag{6}$$

One can find a series of pairs of s and ω that meet (6), which are listed in Table 2. Under the constrain that s is an integer and ω is a positive value, there is no eastward-propagating wave ($s < 0$) that satisfies (6), which is the reason why Table 2 shows only $s \geq 0$.

The waves listed in Table 2 can result from the nonlinear interaction between the Q6DW and migrating tides. It is known that a nonlinear interaction of two global-scale waves, say ($s = s_{w1}$, $\omega = \omega_{w1}$) and ($s = s_{w2}$, $\omega = \omega_{w2}$), leads to the secondary waves with frequencies and zonal wavenumbers that are the sums (+) and differences (−) of those of the interacting waves (Teitelbaum and Vial, 1991). These secondary waves can be expressed as

$$A_{(+)}\cos\left[\left(\omega_{w1} + \omega_{w2}\right)\Omega t_{UT} + \left(s_{w1} + s_{w2}\right)\lambda - \phi_{(+)}\right], \tag{7}$$

and

$$A_{(-)}\cos\left[\left(\omega_{w1} - \omega_{w2}\right)\Omega t_{UT} + \left(s_{w1} - s_{w2}\right)\lambda - \phi_{(-)}\right], \tag{8}$$

where $A_{(+)}$ and $A_{(-)}$ are the amplitude of the secondary waves, while $\phi_{(+)}$ and $\phi_{(-)}$ are the phase. Using Equation (2), these waves are

$$A_{(+)}\cos\left[\left(s_{w1} - \omega_{w1} + s_{w2} - \omega_{w2}\right)\Omega t_{UT} - \phi'_{(+)}\right], \tag{9}$$

and

$$A_{(-)}\cos\left[\left(s_{w1} - \omega_{w1} - s_{w2} + \omega_{w2}\right)\Omega t_{UT} - \phi'_{(-)}\right], \tag{10}$$

where

$$\phi'_{(+)} = \left(s_{w1} + s_{w2}\right)t_{LT}\Omega - \phi_{(+)}, \tag{11}$$

and

$$\phi'_{(-)} = \left(s_{w1} - s_{w2}\right)t_{LT}\Omega - \phi_{(-)}. \tag{12}$$

Table 3
Possible Sources of Westward-Propagating ~6-Day Oscillations With Zonal Wavenumber 1 in PRE Simulated by the TIE-GCM

		Quasi-6-day wave		Secondary waves	
Case #	Case name	Propagation	In situ	Propagation	In situ
(1)	*reference*	○	○	○	○
(2)	*no_PW*		○	○	
(3)	*tides_only*		○	○	
(1)–(2)	*PW_contribution*	○			○
(2)–(3)	*S0_contribution*				

Note. "Secondary waves" here mean those generated by the nonlinear interaction between the quasi-6-day wave and migrating Tides (see also Table 2). The waves in "propagation" are those generated Below the model Lower boundary (97 km), while the waves in "in situ" are those generated locally within the thermosphere above the lower boundary.

By definition, $s = \omega$ for migrating tides. Thus, in the fixed local time frame, the secondary waves due to the nonlinear interaction of the Q6DW and a migrating tide are:

$$A_{(+)}\cos\left[\left(s_6 - \omega_6\right)\Omega t_{UT} - \phi'_{(+)}\right], \tag{13}$$

and

$$A_{(-)}\cos\left[\left(s_6 - \omega_6\right)\Omega t_{UT} - \phi'_{(-)}\right]. \tag{14}$$

It is obvious that these waves cannot be distinguished from the Q6DW itself, which is expressed as (4) in the fixed local time frame. As a matter of fact, for each wave listed in Table 2, it is possible to find a pair of the Q6DW and a migrating tide that could be the source, as indicated in Table 2. In our TIE-GCM simulations, these secondary waves are included in the TIME-GCM/MERRA lower boundary in all three cases (Table 1). Additionally, these waves can be locally generated above the lower boundary (97 km) through the Q6DW interaction with migrating tides in the *reference* simulation but not in the *no_PW* and *tides_only* simulations.

The Q6DW at ionospheric heights is not only by those which propagate from the MLT region but also by those locally generated in the thermosphere through the second-stage nonlinear interaction (Forbes et al., 2018a, 2018b). For example, the nonlinear interaction between the Q6DW ($s = +1$, $\omega = \omega_6$) and eastward-propagating diurnal tide with zonal wavenumber 3 ($s = -3$, $\omega = 1$), DE3, would produce the secondary waves ($s = 1 \mp 3$, $\omega = \omega_6 \pm 1$). If these secondary waves generated below the MLT region enter the thermosphere and go through the nonlinear interaction with DE3 therein, the Q6DW would be locally generated. In this way, the Q6DW could be produced within the thermosphere without the need for the Q6DW spectrum.

To summarize the argument above, ~6-day oscillations of PRE (Figure 4b) can arise from the Q6DW or the secondary waves generated by the nonlinear interaction between the Q6DW and migrating tides. In both cases, the source wave could either propagate from below or be generated within the thermosphere. Table 3 shows which source waves are included in our simulation results. In the *PW_contribution* case, which showed the largest contribution to the Q6DW signature of PRE in Figure 5, ~6-day oscillations can result from the propagation of the Q6DW from the model lower boundary (97 km) or from the secondary waves generated above the lower boundary. In the *tides_only* simulation, ~6-day oscillations of PRE can be due to the Q6DW generated in the thermosphere or due to the propagation of the secondary waves from the lower boundary. In the *S0_contribution* case, no source wave is expected for ~6-day oscillations of PRE from the mechanisms discussed here. Indeed, ~6-day oscillations of PRE are small in the *S0_contribution* case (Figure 5c).

Figure 6 shows the height versus latitude distributions of the amplitudes of the Q6DW and secondary waves for DoY = 267–284, when ~6-day oscillations of PRE are most prominent (Figure 4b). The first row of Figure 6 compares the zonal wind components of the Q6DW obtained from the *reference*, *PW_contribution*, and *tides_only* cases; the second row compares the meridional wind components of the westward-propagating ~21h wave with zonal wavenumber 2 (21hW2), which is a secondary wave due to the nonlinear interaction of the Q6DW and migrating diurnal tide (DW1); and the third row compares the meridional wind components of the westward-propagating ~11h wave with zonal wavenumber 3 (11hW3), which is a secondary wave due to the nonlinear interaction of the Q6DW and migrating semidiurnal tide (SW2). The zonal wind components of 21hW2 and 11hW3 are in the same order of magnitude but tend to be smaller than the meridional wind components.

The comparison of Figures 6a, 6d, and 6g suggests that below 120 km or so, the Q6DW is dominated by the wave that propagate from the lower boundary of the model (as represented in the *PW_contribution* case), and above these heights, the Q6DW locally generated in the thermosphere (as represented in the *tides_only*

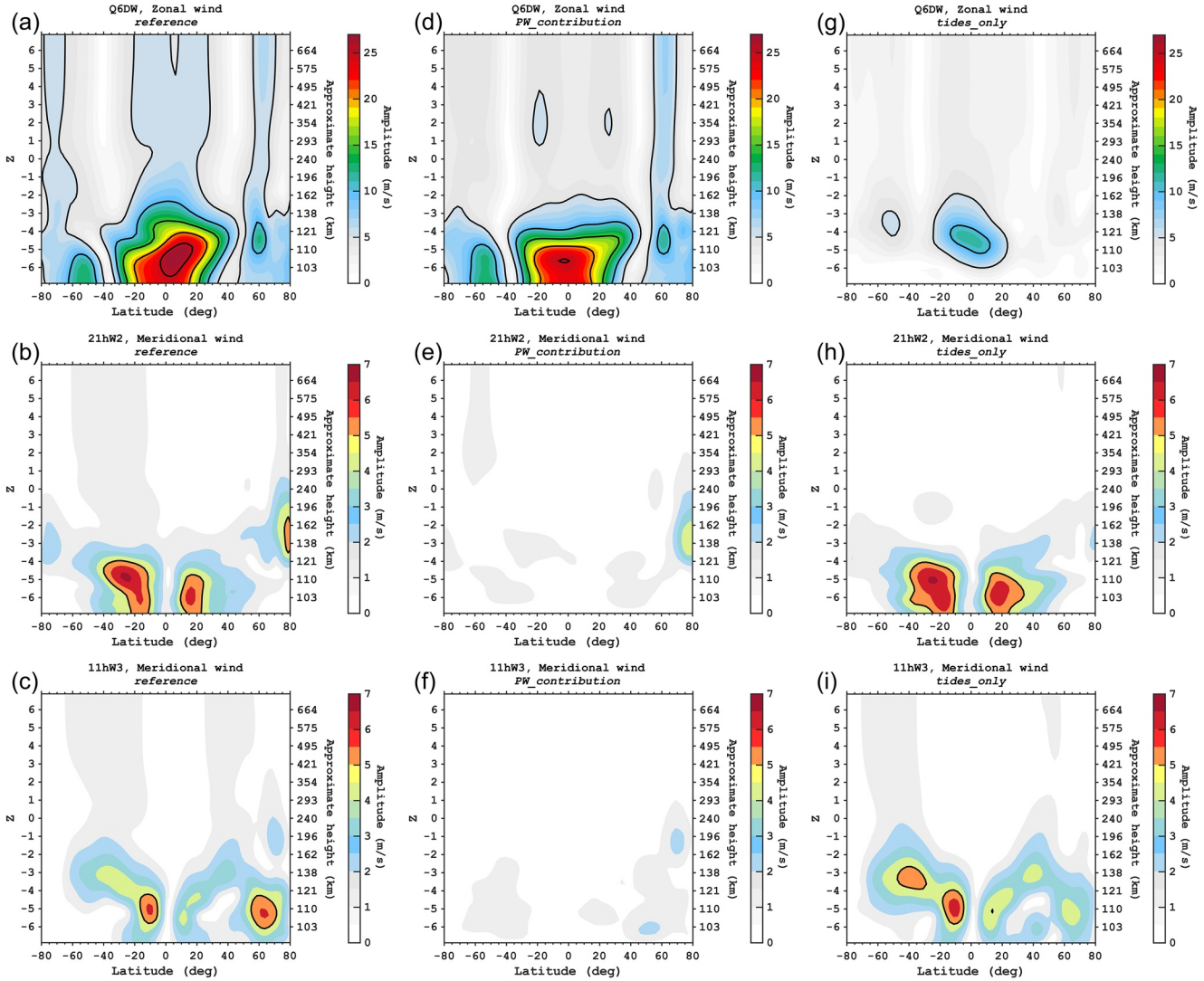

Figure 6. Latitude versus height plots for (a) the zonal wind amplitude of the westward-propagating quasi-6-day wave (Q6DW) with zonal wavenumber 1, (b) the meridional wind amplitude of the westward-propagating ~21 h wave with zonal wavenumber 2 (21hW2), and (c) the meridional wind amplitude of the westward-propagating ~11h wave with zonal wavenumber 3 (11hW3). Note that 21hW2 is a secondary wave due to the nonlinear interaction between the Q6DW and migrating diurnal tide (DW1), while 11hW3 is a secondary wave due to the nonlinear interaction between the Q6DW and migrating semidiurnal tide (SW2). See Table 2 for secondary waves due to the nonlinear interaction between the Q6DW and migrating tides. Panels (d–f) are the same as (a–c) but for the *PW_contribution* case, while panels (g–i) are for the *tides_only* case. See Table 1 for the description of different simulation cases.

simulation) is equally important. For the secondary waves, the waves generated above the model lower boundary (Figures 6e and 6f) do not have as large amplitudes as those which propagate from the lower boundary (Figures 6h and 6i). Similar results are obtained for other secondary waves resulting from the nonlinear interaction between the Q6DW and migrating tides (not shown here).

The primary source of the ~6-day oscillations in PRE during DoY = 267–284 is likely to be the Q6DW that propagate from 97 km based on the fact that (1) the *PW_contribution* case shows larger ~6-day oscillations in PRE than the *tides_only* simulation (Figure 5) and that (2) secondary waves due to Q6DW-tidal interactions are small in the *PW_contribution* case (Figures 6e and 6f). This is unexpected as previous studies (e.g., Abdu et al., 2006a) often suspected that planetary-wave oscillations in PRE are due to tidal modulation by planetary waves rather than due to planetary waves themselves. Nonetheless, the fact that the removal of planetary-wave forcing at the lower boundary does not completely eliminate ~6-day oscillations of PRE (Figures 3c, 3f and 5a) suggests that the Q6DW locally generated in the thermosphere and the upward-propagation of the secondary waves from 97 km also make contributions to Q6DW signatures of PRE.

In summary, the ~6-day variations in PRE intensity around DoY = 270–280, whose amplitudes are 6.0 ± 2.4 m/s from the ground-observer perspective, are dominated by the W1 component, which accounts for up to 4.3 m/s. The rest is mainly due to the W2 and E1 components. Within the W1 component, the Q6DW that propagate from the lower thermosphere is dominant, accounting for up to 3.0 m/s, and the rest is due to the Q6DW locally generated in the thermosphere and the secondary waves associated with the Q6DW-tidal interaction that propagate from below.

Although this study predicts Q6DW effects on the intensity of PRE, the mechanism by which the wave alters PRE V_Z remains to be investigated in future studies. The main driver of PRE is the zonal wind in the F region, but the F-region meridional wind and E-region zonal wind are also known to make nonnegligible contributions to PRE (Du & Stening, 1999; Maute et al., 2012; Millward et al., 2001). Richmond et al. (2015) demonstrated that daytime winds, which are the main driver of the daytime dynamo electric field, have little impact on PRE. Thus, the driving mechanism for the Q6DW effect on PRE can be different from that for the Q6DW effect on the daytime equatorial electrojet intensity and low-latitude F-region plasma density, which has been previously studied (e.g., Miyoshi & Yamazaki, 2020). More numerical work is needed.

5. Conclusions

We have examined temporal and longitudinal variations of the PRE in the equatorial F-region vertical plasma drift using idealized simulations by the TIE-GCM. Simulations were run under geomagnetically quiet ($Kp = 1$) and high solar-flux ($F_{10.7} = 200$) conditions, with realistic atmospheric forcing by large-scale waves based on the TIME-GCM/MERRA output for the year 2009. The main focus of the study was on planetary-wave influences on PRE, which have been previously inferred from local observations (e.g., Abdu et al., 2006a) but have not been evaluated on a global basis. Results and conclusions are as follows:

1. In response to forcing by large-scale waves, PRE shows day-to-day variability in both its intensity (5.6 ± 1.0 m/s in standard deviation) and local time (7.9 ± 3.6 min in standard deviation).
2. The seasonal and longitudinal dependence of the PRE intensity is consistent with that of the angle between the sunset terminator and magnetic meridian, as reported in previous studies. The seasonal and longitudinal dependence of the PRE local time is controlled by the E-region sunset time, in agreement with observations.
3. Day-to-day variations of the PRE intensity at a fixed longitude is predominantly due to tidal-wave forcing (periods less than 2 days). Planetary-wave forcing (periods longer than 2 days) plays a role for periodic oscillations in the PRE intensity, especially those at a period of ~6 days.
4. Zonal-wavenumber analysis of planetary-wave oscillations (2–20 days) in the PRE intensity reveals westward-propagating ~6-day oscillations with zonal wavenumber 1 during times of enhanced quasi-6-day wave (Q6DW) activity.
5. The ~6-day oscillations in the PRE intensity are mainly due to the Q6DW that are generated below the lower boundary of the model (97 km) and propagate into ionospheric heights.
6. The ~6-day oscillations in the PRE intensity are also due in part to the Q6DW locally generated in the thermosphere above 97 km and the secondary waves generated through the nonlinear interaction between the Q6DW and migrating tides.
7. In the example of the Q6DW event around DoY = 270–280, the amplitude of ~6-day variation in the PRE intensity is 6.0 ± 2.4 m/s at a fixed longitude. The westward-propagating zonal wavenumber 1 component explains up to 4.3 m/s, within which the contribution of the Q6DW that propagate from the lower thermosphere accounts for up to 3.0 m/s.

Since the PRE intensity has a strong impact on the occurrence of equatorial spread F and plasma bubbles, planetary-wave oscillations of PRE should be taken into account in the prediction of these space weather phenomena. The zonal wavenumber 1 nature of the ~6-day oscillations could contribute to longitudinal differences in the appearance of equatorial spread F and plasma bubbles.

Data Availability Statement

The simulation data for the intensity and local time of PRE V_Z used in this study are available at https://doi.org/10.5880/GFZ.2.3.2021.001. Software for computing sunset times is available at https://github.com/beaudu/sunrise. This work was supported in part by Deutsche Forschungsgemeinschaft (DFG) grant YA-574-3-1.

Acknowledgments
The authors thank High-Altitude Observatory (HAO) in Boulder, Colorado, USA for providing the TIEGCM code, and associated files for download on https://www.hao.ucar.edu/modeling/tgcm/. We thank Dr. Astrid Maute at HAO for providing the TIEGCM-ICON code, the lower boundary dataset and advice about their use.

References

Abdu, M., Batista, P., Batista, I., Brum, C., Carrasco, A., & Reinisch, B. (2006a). Planetary wave oscillations in mesospheric winds, equatorial evening prereversal electric field and spread F. *Geophysical Research Letters*, *33*(7). https://doi.org/10.1029/2005GL024837

Abdu, M., Bittencourt, J., & Batista, I. (1981). Magnetic declination control of the equatorial F region dynamo electric field development and spread F. *Journal of Geophysical Research*, *86*(A13), 11443–11446. https://doi.org/10.1029/JA086iA13p11443

Abdu, M., Ramkumar, T., Batista, I., Brum, C., Takahashi, H., Reinisch, B., et al. (2006b). Planetary wave signatures in the equatorial atmosphere–ionosphere system, and mesosphere-E- and F-region coupling. *Journal of Atmospheric and Solar-Terrestrial Physics*, *68*(3–5), 509–522.

Batista, I., Abdu, M., & Bittencourt, J. (1986). Equatorial F region vertical plasma drifts: Seasonal and longitudinal asymmetries in the American sector. *Journal of Geophysical Research*, *91*(A11), 12055–12064. https://doi.org/10.1029/JA091iA11p12055

Bertoni, F., Sahai, Y., Raulin, J.-P., Fagundes, P., Pillat, V., de Castro, C. G., et al. (2011). Equatorial spread-F occurrence observed at two near equatorial stations in the Brazilian sector and its occurrence modulated by planetary waves. *Journal of Atmospheric and Solar-Terrestrial Physics*, *73*(4), 457–463.

Blanc, M., & Richmond, A. (1980). The ionospheric disturbance dynamo. *Journal of Geophysical Research*, *85*(A4), 1669–1686. https://doi.org/10.1029/JA085iA04p01669

de Abreu, A., Fagundes, P., Bolzan, M., de Jesus, R., Pillat, V., Abalde, J., et al. (2014). The role of the traveling planetary wave ionospheric disturbances on the equatorial F region post-sunset height rise during the last extreme low solar activity and comparison with high solar activity. *Journal of Atmospheric and Solar-Terrestrial Physics*, *113*, 47–57.

Du, J., & Stening, R. (1999). Simulating the ionospheric dynamo–II. equatorial electric fields. *Journal of Atmospheric and Solar-Terrestrial Physics*, *61*(12), 925–940.

Eccles, J. (1998). Modeling investigation of the evening prereversal enhancement of the zonal electric field in the equatorial ionosphere. *Journal of Geophysical Research*, *103*(A11), 26709–26719. https://doi.org/10.1029/98JA02656

Eccles, J., St Maurice, J., & Schunk, R. (2015). Mechanisms underlying the prereversal enhancement of the vertical plasma drift in the low-latitude ionosphere. *Journal of Geophysical Research: Space Physics*, *120*(6), 4950–4970. https://doi.org/10.1002/2014JA020664

Farley, D., Bonelli, E., Fejer, B., & Larsen, M. (1986). The prereversal enhancement of the zonal electric field in the equatorial ionosphere. *Journal of Geophysical Research*, *91*(A12), 13723–13728. https://doi.org/10.1029/JA091iA12p13723

Fejer, B., De Paula, E., Gonzalez, S., & Woodman, R. (1991). Average vertical and zonal F region plasma drifts over Jicamarca. *Journal of Geophysical Research*, *96*(A8), 13901–13906. https://doi.org/10.1029/91JA01171

Fejer, B., Jensen, J., & Su, S.-Y. (2008a). Quiet time equatorial F region vertical plasma drift model derived from ROCSAT-1 observations. *Journal of Geophysical Research*, *113*(A5). https://doi.org/10.1029/2007JA012801

Fejer, B., Jensen, J., & Su, S.-Y. (2008b). Seasonal and longitudinal dependence of equatorial disturbance vertical plasma drifts. *Geophysical Research Letters*, *35*(20). https://doi.org/10.1029/2008GL035584

Fejer, B., & Scherliess, L. (1997). Empirical models of storm time equatorial zonal electric fields. *Journal of Geophysical Research*, *102*(A11), 24047–24056. https://doi.org/10.1029/97JA02164

Fejer, B., & Scherliess, L. (2001). On the variability of equatorial F-region vertical plasma drifts. *Journal of Atmospheric and Solar-Terrestrial Physics*, *63*(9), 893–897.

Fejer, B., Scherliess, L., & De Paula, E. (1999). Effects of the vertical plasma drift velocity on the generation and evolution of equatorial spread F. *Journal of Geophysical Research*, *104*(A9), 19859–19869. https://doi.org/10.1029/1999JA900271

Fesen, C., Crowley, G., Roble, R., Richmond, A., & Fejer, B. (2000). Simulation of the pre-reversal enhancement in the low latitude vertical ion drifts. *Geophysical Research Letters*, *27*(13), 1851–1854. https://doi.org/10.1029/2000GL000061

Forbes, J. (1995). Tidal and planetary waves. The upper mesosphere and lower thermosphere: A review of experiment and theory. *Geophysical Monograph Series*, *87*, 67–87.

Forbes, J., Maute, A., Zhang, X., & Hagan, M. (2018a). Oscillation of the ionosphere at planetary-wave periods. *Journal of Geophysical Research: Space Physics*, *123*(9), 7634–7649. https://doi.org/10.1029/2018JA025720

Forbes, J., & Zhang, X. (2017). The quasi-6 day wave and its interactions with solar tides. *Journal of Geophysical Research: Space Physics*, *122*(4), 4764–4776. https://doi.org/10.1002/2017JA023954

Forbes, J., Zhang, X., Maute, A., & Hagan, M. (2018b). Zonally symmetric oscillations of the thermosphere at planetary wave periods. *Journal of Geophysical Research: Space Physics*, *123*(5), 4110–4128. https://doi.org/10.1002/2018JA025258

Gan, Q., Eastes, R., Burns, A., Wang, W., Qian, L., Solomon, S., et al. (2020). New observations of large-scale waves coupling with the ionosphere made by the GOLD mission: Quasi-16-day wave signatures in the F-region OI 135.6-nm nightglow during sudden stratospheric warmings. *Journal of Geophysical Research: Space Physics*, *125*(4). e2020JA027880. https://doi.org/10.1029/2020JA027880

Gan, Q., Oberheide, J., & Pedatella, N. M. (2018). Sources, sinks, and propagation characteristics of the quasi 6-day wave and its impact on the residual mean circulation. *Journal of Geophysical Research: Atmospheres*, *123*(17), 9152–9170. https://doi.org/10.1029/2018JD028553

Gan, Q., Oberheide, J., Yue, J., & Wang, W. (2017). Short-term variability in the ionosphere due to the nonlinear interaction between the 6 day wave and migrating tides. *Journal of Geophysical Research: Space Physics*, *122*(8), 8831–8846. https://doi.org/10.1002/2017JA023947

Gan, Q., Wang, W., Yue, J., Liu, H.-L., Chang, L., Zhang, S., et al. (2016). Numerical simulation of the 6 day wave effects on the ionosphere: Dynamo modulation. *Journal of Geophysical Research: Space Physics*, *121*(10), 10–103. https://doi.org/10.1002/2016JA022907

Ghosh, P., Otsuka, Y., Mani, S., & Shinagawa, H. (2020). Day-to-day variation of pre-reversal enhancement in the equatorial ionosphere based on GAIA model simulations. *Earth Planets and Space*, *72*(1), 1–8.

Gu, S.-Y., Ruan, H., Yang, C.-Y., Gan, Q., Dou, X., & Wang, N. (2018). The morphology of the 6-day wave in both the neutral atmosphere and F region ionosphere under solar minimum conditions. *Journal of Geophysical Research: Space Physics*, *123*(5), 4232–4240. https://doi.org/10.1029/2018JA025302

Heelis, R. (2004). Electrodynamics in the low and middle latitude ionosphere: A tutorial. *Journal of Atmospheric and Solar-Terrestrial Physics*, *66*(10), 825–838.
Heelis, R., Crowley, G., Rodrigues, F., Reynolds, A., Wilder, R., Azeem, I., et al. (2012). The role of zonal winds in the production of a pre-reversal enhancement in the vertical ion drift in the low latitude ionosphere. *Journal of Geophysical Research*, *117*(A8). https://doi.org/10.1029/2012JA017547
Heelis, R., Kendall, P., Moffett, R., Windle, D., & Rishbeth, H. (1974). Electrical coupling of the E-and F-regions and its effect on F-region drifts and winds. *Planetary and Space Science*, *22*(5), 743–756.
Huang, C.-S., & Hairston, M. (2015). The postsunset vertical plasma drift and its effects on the generation of equatorial plasma bubbles observed by the C/NOFS satellite. *Journal of Geophysical Research: Space Physics*, *120*(3), 2263–2275. https://doi.org/10.1002/2014JA020735
Hysell, D., & Burcham, J. (2002). Long term studies of equatorial spread F using the JULIA radar at Jicamarca. *Journal of Atmospheric and Solar-Terrestrial Physics*, *64*(12–14), 1531–1543.
Jin, H., Miyoshi, Y., Fujiwara, H., Shinagawa, H., Terada, K., Terada, N., et al. (2011). Vertical connection from the tropospheric activities to the ionospheric longitudinal structure simulated by a new Earth's whole atmosphere-ionosphere coupled model. *Journal of Geophysical Research*, *116*(A1). https://doi.org/10.1029/2010JA015925
Kelley, M., Fejer, B., & Gonzales, C. (1979). An explanation for anomalous equatorial ionospheric electric fields associated with a northward turning of the interplanetary magnetic field. *Geophysical Research Letters*, *6*(4), 301–304. https://doi.org/10.1029/GL006i004p00301
Kil, H., & Oh, S.-J. (2011). Dependence of the evening prereversal enhancement of the vertical plasma drift on geophysical parameters. *Journal of Geophysical Research*, *116*(A5). https://doi.org/10.1029/2010JA016352
Kil, H., Paxton, L., & Oh, S.-J. (2009). Global bubble distribution seen from ROCSAT-1 and its association with the evening prereversal enhancement. *Journal of Geophysical Research*, *114*(A6). https://doi.org/10.1029/2008JA013672
Koval, A., Gavrilov, N., Pogoreltsev, A., & Shevchuk, N. (2018). Influence of solar activity on penetration of traveling planetary-scale waves from the troposphere into the thermosphere. *Journal of Geophysical Research: Space Physics*, *123*(8), 6888–6903. https://doi.org/10.1029/2018JA025680
Lin, J., Lin, C., Rajesh, P., Yue, J., Lin, C., & Matsuo, T. (2020). Local-time and vertical characteristics of quasi-6-day oscillation in the ionosphere during the 2019 antarctic sudden stratospheric warming. *Geophysical Research Letters*. e2020GL090345. https://doi.org/10.1029/2020GL090345
Liu, H.-L. (2016). Variability and predictability of the space environment as related to lower atmosphere forcing. *Space Weather*, *14*(9), 634–658.
Liu, H.-L. (2020). Day-to-day variability of prereversal enhancement in the vertical ion drift in response to large-scale forcing from the lower atmosphere. *Space Weather*, *18*(4). e2019SW002334
Liu, H.-L., Bardeen, C., Foster, B., Lauritzen, P., Liu, J., Lu, G., et al. (2018). Development and validation of the whole atmosphere community climate model with thermosphere and ionosphere extension (WACCM-X 2.0). *Journal of Advances in Modeling Earth Systems*, *10*(2), 381–402.
Liu, H.-L., Talaat, E., Roble, R., Lieberman, R., Riggin, D., & Yee, J.-H. (2004). The 6.5-day wave and its seasonal variability in the middle and upper atmosphere. *Journal of Geophysical Research*, *109*(D21). https://doi.org/10.1029/2004JD004795
Lühr, H., & Manoj, C. (2013). The complete spectrum of the equatorial electrojet related to solar tides: Champ observations. *Annales Geophysicae*. *31*, 1315–1331.
Madhav Haridas, M., Manju, G., & Pant, T. (2015). On the solar activity variations of nocturnal F region vertical drifts covering two solar cycles in the Indian longitude sector. *Journal of Geophysical Research: Space Physics*, *120*(2), 1445–1451. https://doi.org/10.1002/2014JA020561
Manju, G., & Aswathy, R. (2020). Ionospheric planetary wave activity and its role in equatorial spread f day-to-day variability. *Journal of Geophysical Research: Space Physics*, *125*(9), e2020JA027960. https://doi.org/10.1029/2020JA027960
Maute, A. (2017). Thermosphere-ionosphere-electrodynamics general circulation model for the ionospheric connection explorer: TIEGCM-ICON. *Space Science Reviews*, *212*(1–2), 523–551.
Maute, A., Richmond, A., & Roble, R. (2012). Sources of low-latitude ionospheric E×B drifts and their variability. *Journal of Geophysical Research*, *117*(A6). https://doi.org/10.1029/2011JA017502
Millward, G., Müller-Wodarg, I., Aylward, A., Fuller-Rowell, T., Richmond, A., & Moffett, R. (2001). An investigation into the influence of tidal forcing on F region equatorial vertical ion drift using a global ionosphere-thermosphere model with coupled electrodynamics. *Journal of Geophysical Research*, *106*(A11), 24733–24744. https://doi.org/10.1029/2000JA000342
Miyoshi, Y., & Yamazaki, Y. (2020). Excitation mechanism of ionospheric 6-day oscillation during the 2019 september sudden stratospheric warming event. *Journal of Geophysical Research: Space Physics*, *125*(9).e2020JA028283. https://doi.org/10.1029/2020JA028283
Nishida, A. (1968). Coherence of geomagnetic DP2 fluctuations with interplanetary magnetic variations. *Journal of Geophysical Research*, *73*(17), 5549–5559. https://doi.org/10.1029/JA073i017p05549
Nystrom, V., Gasperini, F., Forbes, J. M., & Hagan, M. E. (2018). Exploring wave-wave interactions in a general circulation model. *Journal of Geophysical Research: Space Physics*, *123*(1), 827–847. https://doi.org/10.1002/2017JA024984
Oberheide, J., Forbes, J., Häusler, K., Wu, Q., & Bruinsma, S. (2009). Tropospheric tides from 80 to 400 km: Propagation, interannual variability, and solar cycle effects. *Journal of Geophysical Research*, *114*(D1). https://doi.org/10.1029/2009JD012388
Pancheva, D., & Mukhtarov, P. (2010). Strong evidence for the tidal control on the longitudinal structure of the ionospheric f-region. *Geophysical Research Letters*, *37*(14). https://doi.org/10.1029/2010GL044039
Pancheva, D., Mukhtarov, P., Andonov, B., Mitchell, N. J., & Forbes, J. (2009). Planetary waves observed by TIMED/SABER in coupling the stratosphere–mesosphere–lower thermosphere during the winter of 2003/2004: Part 1–comparison with the UKMO temperature results. *Journal of Atmospheric and Solar-Terrestrial Physics*, *71*(1), 61–74.
Qian, L., Burns, A., Emery, B., Foster, B., Lu, G., Maute, A., et al. (2014). The NCAR TIE-GCM: A community model of the coupled thermosphere/ionosphere system. *Modeling the Ionosphere-Thermosphere System*, *201*, 73–83.
Qin, Y., Gu, S.-Y., Dou, X., Gong, Y., Chen, G., Zhang, S., et al. (2019). Climatology of the quasi-6-day wave in the mesopause region and its modulations on total electron content during 2003–2017. *Journal of Geophysical Research: Space Physics*, *124*(1), 573–583. https://doi.org/10.1029/2018JA025981
Richmond, A. (1995). Ionospheric electrodynamics using magnetic apex coordinates. *Journal of Geomagnetism and Geoelectricity*, *47*(2), 191–212.
Richmond, A. D. (1995). Ionospheric electrodynamics. In H. Volland (Ed.), *Handbook of Atmospheric Electrodynamics*, (Vol. 2, pp. 249–290). Boca Raton, Fla: CRC Press.
Richmond, A., Fang, T.-W., & Maute, A. (2015). Electrodynamics of the equatorial evening ionosphere: 1. Importance of winds in different regions. *Journal of Geophysical Research: Space Physics*, *120*(3), 2118–2132. https://doi.org/10.1002/2014JA020934

Richmond, A., Ridley, E., & Roble, R. (1992). A thermosphere/ionosphere general circulation model with coupled electrodynamics. *Geophysical Research Letters*, *19*(6), 601–604. https://doi.org/10.1029/92GL00401

Rienecker, M., Suarez, M., Gelaro, R., Todling, R., Bacmeister, J., Liu, E., et al. (2011). MERRA: NASA's modern-era retrospective analysis for research and applications. *Journal of Climate*, *24*(14), 3624–3648.

Rishbeth, H. (1971). The F-layer dynamo. *Planetary and Space Science*, *19*(2), 263–267.

Roble, R., & Ridley, E. (1994). A thermosphere-ionosphere-mesosphere-electrodynamics general circulation model (TIME-GCM): Equinox solar cycle minimum simulations (30–500 km). *Geophysical Research Letters*, *21*(6), 417–420. https://doi.org/10.1029/93GL03391

Salby, M. (1984). Survey of planetary-scale traveling waves: The state of theory and observations. *Reviews of Geophysics*, *22*(2), 209–236.

Scherliess, L., & Fejer, B. (1999). Radar and satellite global equatorial F region vertical drift model. *Journal of Geophysical Research*, *104*(A4), 6829–6842. https://doi.org/10.1029/1999JA900025

Stolle, C., Lühr, H., & Fejer, B. (2008). Relation between the occurrence rate of ESF and the equatorial vertical plasma drift velocity at sunset derived from global observations. *Annales Geophysicae*, *26*, 3979–3988.

Stoneback, R., Heelis, R., Burrell, A., Coley, W., Fejer, B. G., & Pacheco, E. (2011). Observations of quiet time vertical ion drift in the equatorial ionosphere during the solar minimum period of 2009. *Journal of Geophysical Research*, *116*(A12). https://doi.org/10.1029/2011JA016712

Talaat, E., Yee, J.-H., & Zhu, X. (2001). Observations of the 6.5-day wave in the mesosphere and lower thermosphere. *Journal of Geophysical Research*, *106*(D18), 20715–20723.

Thébault, E., Finlay, C., Beggan, C., Alken, P., Aubert, J., Barrois, O., et al. (2015). International geomagnetic reference field: The 12th generation. *Earth Planets and Space*, *67*(1), 79.

Tsunoda, R. (1985). Control of the seasonal and longitudinal occurrence of equatorial scintillations by the longitudinal gradient in integrated E region Pedersen conductivity. *Journal of Geophysical Research*, *90*(A1), 447–456. https://doi.org/10.1029/JA090iA01p00447

Vichare, G., & Richmond, A. (2005). Simulation study of the longitudinal variation of evening vertical ionospheric drifts at the magnetic equator during equinox. *Journal of Geophysical Research*, *110*(A5). https://doi.org/10.1029/2004JA010720

Woodman, R. (1970). Vertical drift velocities and east-west electric fields at the magnetic equator. *Journal of Geophysical Research*, *75*(31), 6249–6259. https://doi.org/10.1029/JA075i031p06249

Wu, D., Hays, P., & Skinner, W. (1994). Observations of the 5-day wave in the mesosphere and lower thermosphere. *Geophysical Research Letters*, *21*(24), 2733–2736. https://doi.org/10.1029/94GL02660

Wu, D., Hays, P., Skinner, W., Marshall, A., Burrage, M., Lieberman, R., et al. (1993). Observations of the quasi 2-day wave from the high resolution Doppler imager on UARS. *Geophysical Research Letters*, *20*(24), 2853–2856. https://doi.org/10.1029/93GL03008

Yamazaki, Y. (2018). Quasi-6-day wave effects on the equatorial ionization anomaly over a solar cycle. *Journal of Geophysical Research: Space Physics*, *123*(11), 9881–9892. https://doi.org/10.1029/2018JA026014

Yamazaki, Y., & Dieval, C. (2021). *TIE-GCM simulation data for the equatorial F region vertical plasma drift*. GFZ Data Services. https://doi.org/10.5880/GFZ.2.3.2021.001

Yamazaki, Y., Matthias, V., Miyoshi, Y., Stolle, C., Siddiqui, T., Kervalishvili, G., et al. (2020). September 2019 Antarctic sudden stratospheric warming: Quasi-6-day wave burst and ionospheric effects. *Geophysical Research Letters*, *47*(1). e2019GL086577. https://doi.org/10.1029/2019GL086577

Yamazaki, Y., Stolle, C., Matzka, J., & Alken, P. (2018). Quasi-6-day wave modulation of the equatorial electrojet. *Journal of Geophysical Research: Space Physics*, *123*(5), 4094–4109. https://doi.org/10.1029/2018JA025365

Zhu, Z., Luo, W., Lan, J., & Chang, S. (2017). Features of 3–7-day planetary-wave-type oscillations in F-layer vertical drift and equatorial spread F observed over two low-latitude stations in China. *Annales Geophysicae*, *35*(3), 763–776.